UC San Diego

Title

3D collagen architecture regulates cell adhesion through degradability, thereby controlling metabolic and oxidative stress

Permalink

Journal

ISSN

Authors

Velez, Daniel O
Ranamukhaarachchi, Sural K
Kumar, Aditya
et al.

Publication Date

DOI

Peer reviewed

ORIGINAL ARTICLE

3D collagen architecture regulates cell adhesion through degradability, thereby controlling metabolic and oxidative stress

Daniel O. Velez[1], Sural K. Ranamukhaarachchi[1], Aditya Kumar[1], Rishi N. Modi[1], Esther W. Lim[1], Adam J. Engler[1], Christian M. Metallo[1], and Stephanie I. Fraley[1,2,*]

[1]Bioengineering Department, University of California San Diego, CA, USA and [2]Moore's Cancer Center, University of California San Diego La Jolla, CA, USA

*Corresponding author. E-mail: sifraley@ucsd.edu

Abstract

The collagen-rich tumor microenvironment plays a critical role in directing the migration behavior of cancer cells. 3D collagen architectures with small pores have been shown to confine cells and induce aggressive collective migration, irrespective of matrix stiffness and density. However, it remains unclear how cells sense collagen architecture and transduce this information to initiate collective migration. Here, we tune collagen architecture and analyze its effect on four core cell-ECM interactions: cytoskeletal polymerization, adhesion, contractility, and matrix degradation. From this comprehensive analysis, we deduce that matrix architecture initially modulates cancer cell adhesion strength, and that this results from architecture-induced changes to matrix degradability. That is, architectures with smaller pores are less degradable, and degradability is required for cancer cell adhesion to 3D fibrilar collagen. The biochemical consequences of this 3D low-attachment state are similar to those induced by suspension culture, including metabolic and oxidative stress. One distinction from suspension culture is the induction of collagen catabolism that occurs in 3D low-attachment conditions. Cells also upregulate Snail1 and Notch signaling in response to 3D low-attachment, which suggests a mechanism for the emergence of collective behaviors.

Insight, innovation, integration

Cancer cell interactions with the 3D collagen-rich tumor microenvironment influence several aspects of cell growth, metabolism, and invasion. This study provides an integrative and time-dynamic understanding of how collagen is sensed by cancer cells and can lead to cellular reprogramming. Using a combination of extracellular matrix engineering techniques, biophysical measurements of cell-matrix interactions, as well as biochemical and transcriptional analyses, we find that collagen architectures that are less degradable limit cell adhesion, inducing metabolic and oxidative stress followed by collective migration. These findings lend deeper insight into the initiation of collective cancer cell

(Continued)

(Continued)

behaviors associated with higher metastatic potential and suggest that matrix degradability is a key microenvironmental influence.

Introduction

Collective cancer cell migration is thought to be the predominant means of metastatic dissemination in many solid human tumors [1–3]. In mouse models of cancer metastasis and in 3D *in vitro* tumor models, collectively migrating cells are typically more invasive and are resistant to chemotherapeutics [3–6]. Improved mechanistic understanding of how collective migration is initiated may reveal novel strategies for metastasis treatment or prevention.

We and others have demonstrated that the fibrillar architecture of 3D collagen plays a unique role in inducing collective migration, independently of matrix stiffness and density [7–10]. In previous studies we showed that confining 3D collagen matrices, characterized by short fibril architectures and small pores, induce collective migration after ~36 hours of culture, whereas culture in Matrigel or on top of collagen or Matrigel did not induce collective migration. We also reported a conserved transcriptional state that is associated with the collective migration phenotype and is clinically relevant to patient outcomes in nine human tumor types [9]. However, it remains unclear how cancer cells sense and transduce collagen architecture to 'turn on' the collective phenotype. Here, we sought to address this knowledge gap by determining how collagen architecture regulates key cell-matrix interactions (adhesion, cytoskeletal polymerization, contractility, and matrix remodeling), which are transduced into changes in cellular biochemistry. We focus our study of these processes on the time frame before collective migration is initiated, the first ~36 hr of 3D culture, in order to establish the chain of events that lead to the long-term collective migration phenotype.

By tuning the architecture of collagen using PEG as a molecular crowding agent, which largely avoids changes in stiffness or density, we find that more confining architectures, i.e. shorter fibrils and smaller pores, are less susceptible to degradation by matrix metalloproteinases (MMPs). Further, we show that cell-matrix adhesive coupling relies on matrix degradation in 3D fibrilar collagen. Low-degradability matrices force cells into a state of low adhesion, both biophysically and biochemically, within the first 24 hours of 3D culture. The cellular response to this state is characterized by upregulation of protease activity, collagen catabolism, and Notch signaling, which precedes the transition into collective migration.

Methods

Cell culture

HT-1080 and MDA-MB-231 fibrosarcoma cells were purchased from (ATCC, Manassas, VA) and cultured in high glucose Dulbecco's modified Eagle's medium supplemented with 10% (v/v) fetal bovine serum (FBS, Corning, Corning, NY) and 0.1% gentamicin (Gibco Thermofisher, Waltham, MA) and maintained at 37°C and 5% CO2 in a humidified environment during culture and imaging. The cells were passaged every 2–3 days as required.

Low attachment cultures

For measurements of cell activity under loss of attachment we used low attachment plates (Corning, corning, New York). Cells, were trypsinized from standard cell culture flasks and passage into low attachment plates to a 50–60% confluency. For RNA extraction cells were collected by resuspension in PBS and centrifugation. For metabolism measurements, supernatant was collected from culture and spun down to clear cell debris.

3D culture in collagen I matrix

Cell laden 3D collagen matrices were prepared by mixing cells suspended in culture medium and 10X reconstitution buffer, 1:1 (v/v), with soluble rat tail type I collagen in acetic acid (Corning, Corning, NY) to achieve the desired final concentration [62–64] as described previously by our group. 1 M NaOH was used to normalize pH in a volume proportional to collagen required at each tested concentration (pH 7.0, 10–20 µl 1 M NaOH). Gels were polymerized at 37°C in a humidified incubator. To modify the structure of the collagen fibers to obtain LDSF gels we used a technique previously reported by our group [11]. Briefly, Polyethylene glycol (PEG, MW = 8000, Sigma, St. Louis, MO) was solubilized in phosphate-buffered solution (PBS) and filter sterilized. Solubilized PEG was then mixed into the cells, reconstitution buffer solution described above to produce a final PEG concentration of 10 mg/mL in the collagen gel. The gels were allowed to polymerized in the same conditions as collagen only gels. Collagen structure modification was verified using confocal reflection microscopy.

Collagen gel mechanical properties measurement using shear rheology

To measure the collagen matrix stiffness, we used a shear rheometer (hybrid rheometer (DHR-2) from TA Instruments, New Castle, DE) using a cone and plate geometry with a sample volume of 0.6 ml. Shear storage modulus G′ was measured as reported before [64]. Briefly, we first performed a strain sweep was from 0.1 to 100% strain at a frequency of 1 rad s−1 to determine the elastic region. Then a frequency sweep was performed at a strain within the linear region (0.8%) between 0.1 and 100 rad s−1. Three independent replicates were performed for each condition tested.

Collagen gel stiffness using atomic force microscopy (AFM)

AFM was performed to measure local collagen gel stiffness as previously described [65–67]. Briefly, nano-indentations were performed using a MFP-3D Bio Atomic Force Microscope (Oxford Instruments) mounted on a Ti-U fluorescent inverted microscope (Nikon Instruments). A pyrex-nitride probe with a pyramid tip (nominal spring constants of 0.08 N/m, 35° half-angle opening, and tip radius of 10 nm, NanoAndMore USA Corporation, cat # PNP-TR) was first calibrated for the deflection inverse optical lever sensitivity (Defl InvOLS) by indentation in

PBS on glass followed by using a thermal noise method provided by the Igor 6.34 A software (WaveMetrics) as previously described. Samples were loaded on the AFM, submersed in phosphate buffered saline (PBS), and indented at a velocity of 2 μm/s. Samples were indented until the trigger point, 2 nN, was achieved. Five measurements, equally spaced 50 μm apart, were taken per gel. Tip deflections were converted to indentation force for all samples using their respective tip spring constants and Hooke's Law. Elastic modulus was calculated based on a Hertz-based fit using a built-in code written in the Igor 6.34 A software. The Hertz model used for a pyramidal tip is

$$F = \frac{2}{\pi} \tan(\alpha) \frac{E}{1 - \nu^2} \delta^2 \tag{1}$$

where F is force, α is the half-angle opening of the tip, ν is the Poisson's ratio, E is elastic modulus and δ is indentation. We assumed a Poisson's ratio of 0.5 (incompressible) for all samples. Curves were only analyzed if at least 80% of the fit curve crossed over the data points.

Chemical force spectroscopy

Silicon nitride probes were functionalized as previously described [12, 68]. Probes were cleaned with chloroform for 30 seconds followed by incubation in 5 M ethanolamine-HCL (Sigma) overnight at room temperature. After washing in PBS, tips were incubated in 25 mM bis(sulfosuccinimidyl) suberate (BS3, Thermo Fisher, Waltham, MA) for 30 minutes. Tips were washed in PBS before incubation with 200 μg/mL of recombinant integrin α2β1 heterodimers (R&D Biosystems) for 30 minutes. Probes were washed and air-dried at 4°C until use. Upon use, probes were thermally calibrated as previously described [12, 68]. Force curves were obtained on a 3D-MFP-BIO atomic force microscope (Asylum Research, Santa Barbara, CA) but moving the probe into contact with the material at indentation velocities of 2 μm/s and retracting at the same speed. To allow for adhesion, a 2 second dwell time was added upon probe contact with the surface. Adhesion force during retraction was measured using the Igor Pro 6.34 A software as the maximal negative force on the probe when retracting the tip (Supplemental Figure 1A). As a negative control, poly(ethylene glycol) diacrylate (PEGDA) hydrogels were made by mixing 10% w/v 6 kDa PEGDA (Sigma) with 0.05% Irgacure 2959 (Sigma) and exposing the solution to 350 nm UV light (4 mW/cm [2], UVP) for 5 minutes. Tip interactions with the substrate were thresholded to the non-adhesive PEGDA hydrogels. This value was determined to be 0.5 nN for the probe coated with integrin α2β1. Adhesive interactions were divided by total tip indentations for three different gels for each condition.

Confocal reflection microscopy

Confocal reflection images were acquired and processed as we have previously reported [9]. Briefly, Images were acquired using a Leica SP5 confocal microscope (Buffalo Grove, IL) equipped with a HCX APO L 20 × 1.0 water immersion objective. The sample was excited at 488 nm and reflected light was collected without an emission filter. Collagen fibril length was analyzed using the free software ctFIRE (http://loci.wisc.edu/software/ctfire) [69, 70].

Protrusion Analysis

To monitor actin polymerization activity, HT1080 were stably transduced with Dendra-2-Lifeact (Dendra2-Lifeact-7 was a gift from Michael Davidson (Addgene plasmid # 54 694)). Stably expressing cells were sorted (BD influx, FACS) to select for cell expressing the construct at low levels to avoid off target effects caused by high copy numbers. Cells were embedded into 3D collagen matrices as described above. Timelapse imaging was performed using an inverted confocal microscope equipped with temperature, CO2 and humidity controls for life cell imaging (Olympus FV100).

3D matrix-bound fluorescent bead displacement analysis

To quantify collagen matrix deformations due to cellular forces, fluorescent carboxylate microspheres (1 μm, Thermofisher Scientific, Waltham, MA) were added to the cell-gel solution before polymerization and GFP+ HT1080 cells were used to accurately track cell movements and protrusion extensions. Thoroughly mixed gels were the poured into custom made PDMS wells mounted on glass bottom dishes (Fluorodish, World precision Instruments). The gels were left to polymerize for at least 3 hours and full culture medium was added on top of the gels before imaging started. Imaging was performed using a Nikon TI inverted microscope equipped with a 40X (NA: 1.15) long working distance objective (Nikon Instruments Inc., Melville, NY). For each experiment replicate, between 6–9 cells were randomly selected around the matrix at different depths and a Z stack of images of the beads (red channel) and cells (green channel) was acquired every 0.8 μm, covering 17.5 μm above the cell and 17.5 μm below the cell every 2 minutes for 120 minutes. Offline analysis was performed by generating a extended depth of focus image (EDF) for each time point and tracking individual beads using ImageJ software (NIH, Bethesda, Maryland, USA, https://imagej.nih.gov/ij/). During data collection, special care was taken to select only cells that appeared mostly in polarized in the XY plane to avoid underestimation of Z movements by EDF analysis. We confirmed that the largest deformations imposed by the cells into the matrix happen in the cell plane (XY in this case). Although some information might be lost due to projection to a single plane of a 3D volume our internal controls confirm that deformations happening in the Z directions are significantly smaller than those happening in the XY directions (Supplementary Figure 4C).

Fluorescent beads trajectory analysis

Analysis of individual bead movements as a function of time yielded X,Y coordinates for each bead in the field of view for each time point. Supplementary Figure 3 describes the algorithm followed to extract different metrics from that coordinate data. First, a filter was applied to analyze only trajectories of beads that were picked up by the PIV software at all time points. Thus, beads that became out of focus and impeded proper tracking were discarded. Second, the displacement at each time point from the initial point was calculated for each bead, which yielded trajectories like the ones depicted in Supplementary Figure 3B. Next, to identify beads that were actively pulled by the cells we used a moving standard deviation approach where we calculated the standard deviation of consecutive points across the entire bead trajectory. With this, as can

be visualized in Supplementary Figure 3D-F, we were able to identify the parts of the trajectory that significantly deviated from the rest, which corresponds to a deformation in the matrix. Importantly, when examining the trajectories that are thresholded out using this method versus the ones that are kept, we can see that a bead that is very close to a cellular protrusion, and thus being strongly pulled, is kept (Supplementary Figure 3F), whereas a trajectory that shows only a drift like movement is thresholded out (Supplementary Figure 3E). From the trajectories that passed this threshold we then calculate max bead displacement and cell slip ratio metrics.

Whole cell slip ratio calculation

Slip ratios were calculated as the ration between the instant cell velocity and the surrounding beads instant cell velocity. Cell instant velocity was calculated by tracking single cells using metamorph software (Molecular devices, San Jose, CA). Cell tracking produces x,y coordinates for the cell body at every time-lapse frame and instant velocity is computed as the distance traveled by the cell between consecutive frames. For surrounding beads instant velocity, we tracked the trajectory of all beads in a 165×165 µm square around the cell body using ImageJ's plugin MOSAIC particle tracker (http://mosaic.mpi-cbg. de/?q=downloads/imageJ). For beads trajectories, we performed the same analysis as for cell trajectories to obtain a frame by frame velocity. Slip ratio was calculated as the cell velocity divided by the average of all bead velocities around the cell (Supplementary Figure 2E).

Western blotting from 3D constructs

Whole 200uL 3D collagen constructs from the different culture conditions were scooped out if the well into vials containing 2 mL of PBS and immediately spun down at 1500xg for 5 mins. Supernatant was then discarded and 200 uL of lysis buffer containing proteases and phosphatase inhibitor cocktails was added to the pellets (Thermofisher Scientific, Waltham, MA). The samples were then sonicated on ice for 30 s and immediately after loading buffer containing SDS and DTT was added to get a final 1X concentration. The samples were incubated on ice in loading buffer for 1 h with vortexing every 10–15 mins. After this, the samples are spun down at 12 000xg for 10 mins and then boiled at 95 C for 5 mins. Proteins are separated by SDS-PAGE and transferred to a PVDF membrane. Membranes were probed with antibodies against phosphorylated FAK (44–624 G, Thermofisher) and tubulin (TU-01, thermofisher).

Gene expression using RNA Sequencing

A previously generated RNA Sequencing dataset was used to investigate gene expression changes associated with short fiber architecture [9]. Briefly, total RNA was extracted using Trizol and prepared for sequencing on the Illumina MiSeq platform at a depth of >25 million reads per sample. The read aligner Bowtie2 was used to build an index of the reference human genome hg19 UCSC and transcriptome. Paired-end reads were aligned to this index using Bowtie2 [71] and streamed to eXpress [72] for transcript abundance quantification using command line 'bowtie2 −a −p 10 −x /hg19−1 reads_R1.fastq −2 reads_R2.fastq | express transcripts_hg19.fasta'. For downstream analysis TPM was used as a measure of gene expression.

Gene set enrichment analysis (GSEA)

Gene set enrichment analysis was performed using the Broad institute GSEA tool software.broadinstitute.org/gsea/index.jsp) with standard settings. Rank list were constructed from mean log2 fold change from 2.5 mg/mL to HD culture conditions across 3 biological replicates.

Gene expression analysis using panther database

To identify gene expression programs upregulated in highly confining matrices, we used a gene module previously reported by us that is commonly upregulated to HT1080 fibrosarcoma cells and MDA-MB-231 breast cancer cells cultured in this matrix (HD collagen). The 70 gene module was used as input for panther database analysis (http://www.pantherdb.org/ geneListAnalysis.do) and enrichment test was performed.

Glucose, lactate and glutamine measurements

Medium from the indicated culture conditions was harvested after 24 h of incubation under standard cell culture conditions. Aliquots were spun down at 300xg for 5 min before 100 µL was analyzed using a YSI 2950 Biochemistry Analyzer (YSI, Yellow Springs, OH). Glucose, glutamine, and lactate were measured in the collected samples and in medium incubated under the same conditions but without cells. Consumption and production were calculated as a delta between the experimental samples and the non-cell counterparts.

Gas chromatography–mass spectrometry (GC–MS) sample preparation and analysis

Cells were seeded in LD and HD matrices at a density of 1 M cells/mL and cultured at standard conditions for 24 h. To assess the oxidative pentose phosphate pathway, cells were cultured with [1,2–^{13}C] glucose (Cambridge Isotope Laboratories, Inc.) in glucose-free medium supplemented with 10% (v/v) fetal bovine serum (FBS, Corning, Corning, NY) and 0.1% gentamicin. To determine labeling on metabolites, medium harvested from the indicated culture conditions was centrifuged at 300xg for 5 minutes and 10uL of supernatant was extracted with -20°C methanol/water (8:1, v/v) solution. Samples were then vortexed for 5 minutes and centrifuged at 21 000xg for 5 minutes at 4°C. The upper phase was collected and dried. Derivatization for polar metabolites was performed using a Gerstel MPS with 15uL of 2% (w/v) methoxyamine hydrochloride (Thermo Scientific) in pyridine (incubated for 60 minutes at 45°C) and followed by 15uL N-tertbutyldimethylsilyl-N-methyltrifluoroacetamide (MTBSTFA) with 1% tert-butyldimethylchlorosilane (Regis Technologies) (incubated for 30 minutes at 45°C). Polar derivatives were analyzed by GC-MS using a DB-35MS column (30 m x 0.25 mm i.d. x 0.25 m) installed in an Agilent 7890B gas chromatograph (GC) interfaced with an Agilent 5977B mass spectrometer (MS) with an XTR EI source using the following temperature program: 100°C initial, increase by 3.5°C/min to 255°C, increase by 15°C/min to 320°C and hold for 3 minutes. The % isotopologue distribution of each fatty acid and polar metabolite was determined by integration using in-house MATLAB-based algorithm and corrected for natural abundance using method described in Fernandez et al. [73].

Matrix degradability

In order to measure degradability of the different collagen constructs, we used an approach based on measuring protein rom the different hydrogels in the presence of collagenase, using a BCA assay, as has been described previously [74]. For this, gels 100uL were prepared in 1.5 mL reaction tubes and Collagenase (Sigma, C0130) was prepared at 0.1 mg/mL and added to the collagen gels. The gels were incubated at 37 C and small aliquots were taken from each degradation reaction after a brief centrifugation step. Protein in the collected supernatant was measured using a BCA assay kit (Thermofisher). Degradation rate was calculated using linear regression and assuming a total supernatant volume of 200uL to obtain an absolute protein content measurement at each time point.

DQ collagen degradation assay

Local matrix degradation was measured using DQ collagen (Thermofisher Scientific, Waltham, MA). Briefly, collagen matrices were prepared as described above with 100 ug/mL of DQ collagen mixed in. Cell laden DQ-gels were incubated for 24hs in standard cell culture conditions in the presence of full cell culture medium. 3D gels were imaged using a confocal microscope equipped with a 40X objective (NA:0.75) (Olympus FV100). Zstacks were acquired at a 0.4 µm step size covering the entire cell body. Images were processed offline using ImageJ. DQ intensity was quantified as the mean intensity around the cell body minus the mean intensity of an ROI of the same area in a gel area without cells to account for background DQ signal.

Diffusivity analysis

To assess whether diffusion was limited in more confining matrices (Supplementary Figure 7A-C), we prepared collagen gels as described above and polymerized them inside commercially available rectangular microchannel (µ-Slide VI 0.4, IBIDI, Munich, Germany). 88 µm solutions of fluorescein conjugated dextran were prepared and added to one end of the microchannel while keeping cell growth medium in the other end. The gels were then placed in the stage of a fluorescence microscope and imaged at 1 min intervals for 8 hours to monitor the fluorescence signal as an indicator of dextran concentration along the collagen matrix. Images were then analyzed using matlab and a concentration profile was acquired for each time point. The obtained data was fitted to a 1-D diffusion process using equation 1 and the parameter D extracted.

$$C(t, X) = C_{max} * \left(1 - \text{erf}\left(\frac{X}{2\sqrt{Dt}}\right)\right) \quad (2)$$

where Cmax is the initial concentration at the source and erf is the error function.

Quantitative reverse transcription PCR (RT-qPCR)

For qPCR experiments RNA was extracted using High Pure RNA Isolation Kit (Roche, Basel, Switzerland). cDNA was synthesized using superscript iii first-strand synthesis system (Thermofisher, Waltham, MA). Relative mRNA levels were quantified using pre-designed TaqMan gene expression assays (Thermofisher, Waltham, MA). Relative expression was calculated using the DCt method using GAPDH as reference gene. Assays used were: GAPDH (Hs02758991_g1), MRC2 (Hs00195862_m1).

Results

3D collagen architecture is tuned by molecular crowding

To study the influence of matrix architecture on cancer cell migration, we used a previously developed method to tuned collagen fibril organization independently of altering density and stiffness by molecular crowding with polyethylene glycol (PEG) during polymerization and cell embedding [9, 11]. PEG, an inert crowding agent, was subsequently washed out of the polymerized matrix. Low density 2.5 mg/ml collagen (LD) polymerized in the presence of 10 mg/ml PEG crowding agent (LD_PEG) produced a more confining matrix architecture with short fibrils and small pores, which was similar to a high density HD collagen matrix (HD) in terms of fibril length and pore size (Figure 1A-C) but not mechanical properties (Figure 1D). Bulk as well as local matrix stiffness was measured using shear rheology and atomic force microscopy (AFM), respectively. By shear rheology, we found that the HD matrix was significantly stiffer that the LD and LD_PEG matrices (Figure 1D, left). No differences were detected between the LD and LD_PEG (Figure 1D, left). Using AFM we found statistically significant but small differences in the local stiffness between LD and LD_PEG conditions (Figure 1D, right). However, a larger difference was observed between the LD_PEG and HD conditions (Figure 1D, right). Upon embedding MDA-MB-231 breast cancer or HT-1080 fibrosarcoma cells sparsely in each matrix condition, we observed that cells in LD_PEG or HD matrices underwent a migration transition characterized by rapid, persistent, invasive, and collective cell migration after ~36 hours [9]. This transition was associated with the upregulation of cell-cell adhesion genes PECAM1, ICAM1, CTNNA1, ITGB4, and ITGB5 (Figure 1E-F) and multicellular structure formation in long-term culture over 7 days (Figure 1G). However, in LD matrices where collagen formed long fibrils and large pores, cells migrated individually in a persistent random-walk, mesenchymal migration mode and remain as single cells for the entire observation period of 7days (Figure 1G) [9]. To assess whether, in the event of incomplete PEG removal, cell-collagen interactions were influenced by PEG, we used a force spectroscopy approach [12]. Supplementary Figure 1 demonstrates that even in the presence of excess PEG, there are no significant differences in the ability of integrin heterodimers to bind collagen. Together, these data showed that neither the stiffness nor the density of collagen could explain the observed transition into a collective migration phenotype. Next, we used this model system to study the initial cell-ECM interactions occurring within the first ~36 hr after 3D embedding to understand how matrix architecture triggers the collective phenotype.

Confining architectures reduce protrusion stability

Cells interact with their surrounding matrix using four key biophysical processes: cytoskeletal polymerization, adhesion, contractility, and matrix remodeling. To comprehensively assess the effect of fibril architecture on cell-matrix interactions, we measured each of these processes within the first 1–24 hr after cell embedding. First, we assessed cytoskeletal protrusion dynamics. Time-lapse microscopy of LifeAct-expressing HT-1080 cells in collagen (Figure 1H) revealed that cells in more confining LD_PEG and HD matrices maintained a rounded shape, as shown by cell circularity measured at 8 h (Figure 1I) and by circularity measured as a function of time after 3D embedding (Supplementary Figure 2A). On the other hand, cells in LD
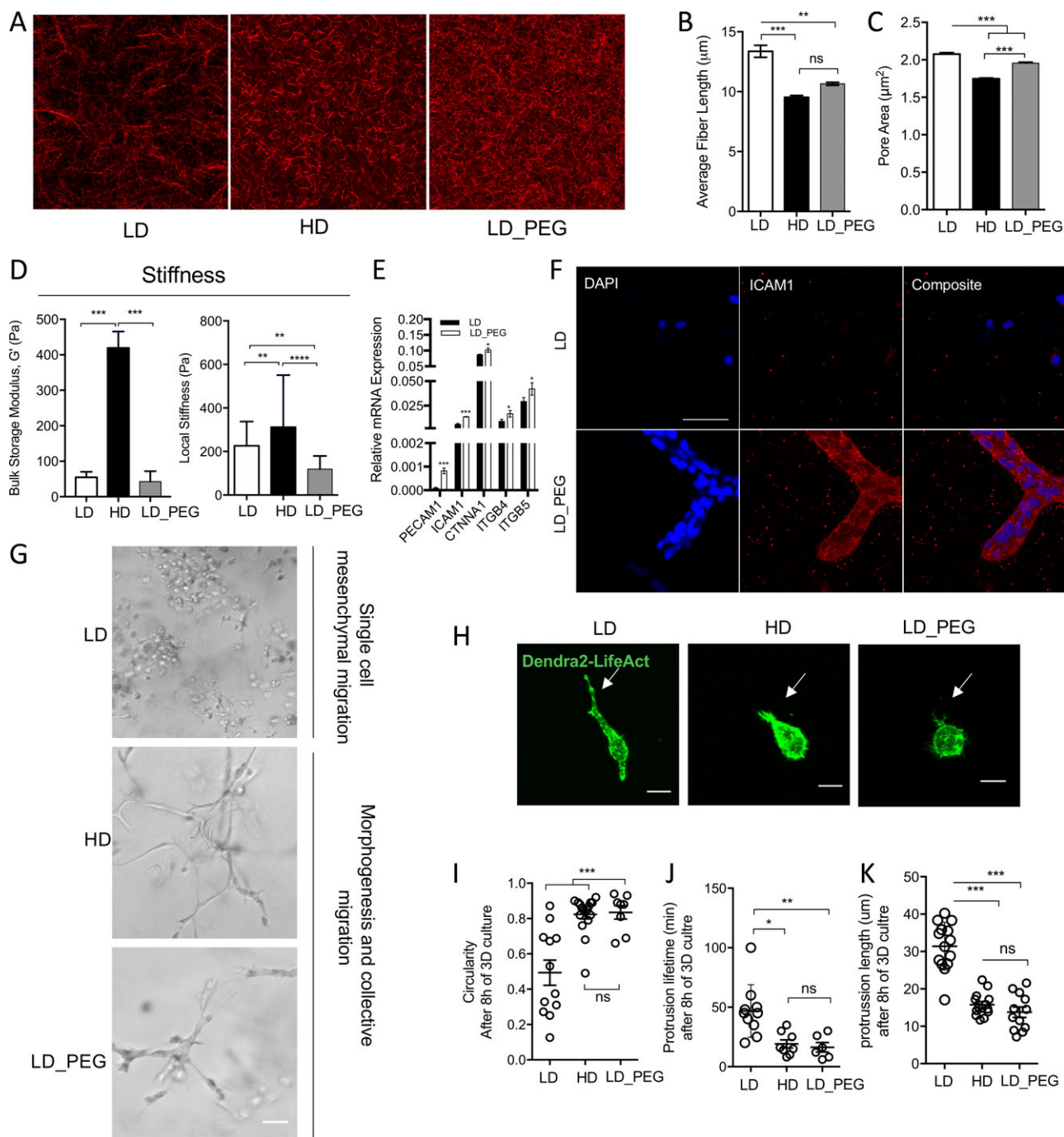
Figure 1. Confining 3D ECM architectures constrain cell spreading and protrusion stabilization. **A.** Confocal reflection images showing the fiber architecture of collagen matrices at 2.5 mg/mL (LD, characterized by low bulk collagen density and long fibers), 6 mg/mL (HD, characterized by high bulk collagen density and short fibers) and 2.5 mg/mL+10 mg/mL PEG (LD_PEG, characterized by low bulk collagen density and short fibers). **B.** Quantification of mean fiber length in the 3 matrix conditions shown in A. **C.** Quantification of pore area in the 3 matrix conditions shown in A. **D.** Stiffness of matrices of the 3 different conditions shown in A as measured by shear rheology (bulk stiffness, left panel) and Atomic Force Microscopy (AFM) (local stiffness, right panel) **E.** RT-qPCR quantification of upregulated cell adhesion genes in LD and LD_PEG conditions. **F.** Immunofluorescent staining of ICAM1 cell-cell adhesion marker in single cell and multicellular morphologies. Scale bar shows 100 μm. **G.** Bright field micrographs of HT-1080 cells cultured in collagen gels for 7 days, scale bar 50 μm. **H.** Dendra2-Lifeact cells show actin polymerization in cellular protrusions in the 3 described matrix conditions. Scale bar 25 μm. **I.** Circularity of cells embedded in the 3 matrix conditions at 8 hours after seeding. **J.** Protrusion lifetime and **K.** length for cells embedded in the 3 matrix conditions. n = 3 biological replicates for each experiment, statistical significance described as *, **, *** for p≤0.05, p≤0.01, p≤0.001 respectively.

matrices took on spindle-shaped mesenchymal morphology rapidly after 3D collagen embedding (Supplementary Figure 2A-B). During the first 8 h of culture, cells in LD_PEG and HD conditions also interacted with the matrix using shorter-lived and smaller protrusions than in the LD matrices (Figure 1J-K). In the LD matrix, where fibril lengths averaged 13.5 μm, protrusions extended to 31.4 μm and lasted for 46 min on average. On the other hand, in LD_PEG and HD matrices having average fibril lengths of 9.5 and

10 μm respectively, protrusions extended to 15.7 and 13.7 μm and lasted 19 and 16 min on average. No statistically significant differences were observed between cells in LD_PEG and HD conditions. Collectively, these results suggested that matrix architectures with small pores and short fibers confined cells to a rounded shape and altered protrusion dynamics independently of matrix stiffness or bulk collagen density.

Confining matrix architectures destabilize cell adhesion

Since we observed small and short-lived protrusions in LD_PEG and HD architectures where cells remained rounded, we hypothesized that these protrusions were less stable in their adhesion to and contraction of the matrix. Simultaneous confocal reflection imaging of collagen fibrils and the cell protrusions in the LD_PEG and HD conditions showed that cells were primarily moving without causing large matrix deformations (Supplementary videos 2–3). On the other hand, cells in the LD condition showed significant pulling and displacement of fibrils (Supplementary Figure 2B and Supplementary video 1).

To quantitatively assess the ability of cells to adhere to and contract the matrix, we embedded GFP-expressing HT-1080 cells in each matrix condition along with carboxylated fluorescent microspheres, which covalently bind to collagen fibrils and allow for high resolution, time-resolved tracking of cell traction by simultaneously monitoring bead and cell movements (Figure 2A, Supplementary Figure 2C and Methods). Quantification of the maximum bead displacement (Supplementary Figure 2D) by cells in each condition during the first 8 h of culture revealed significantly less matrix deformation in the LD_PEG and HD matrices compared to the LD condition (Figure 2B).

Further detailed analysis of protrusion and matrix movement (Figure 2C) revealed that in the LD architecture, cellular protrusions and matrix deformations were well coordinated, producing large bead displacements (See Methods and Supplementary Figure 3 and 4). This phenotype was characterized by high matrix pulling even when the cell's protrusion displays little local movement and is not visually translocating, also known as treadmilling (Figure 2C). However, cells in the more confining LD_PEG and HD matrices erratically pushed, pulled, and lost attachment to the matrix as their short-lived
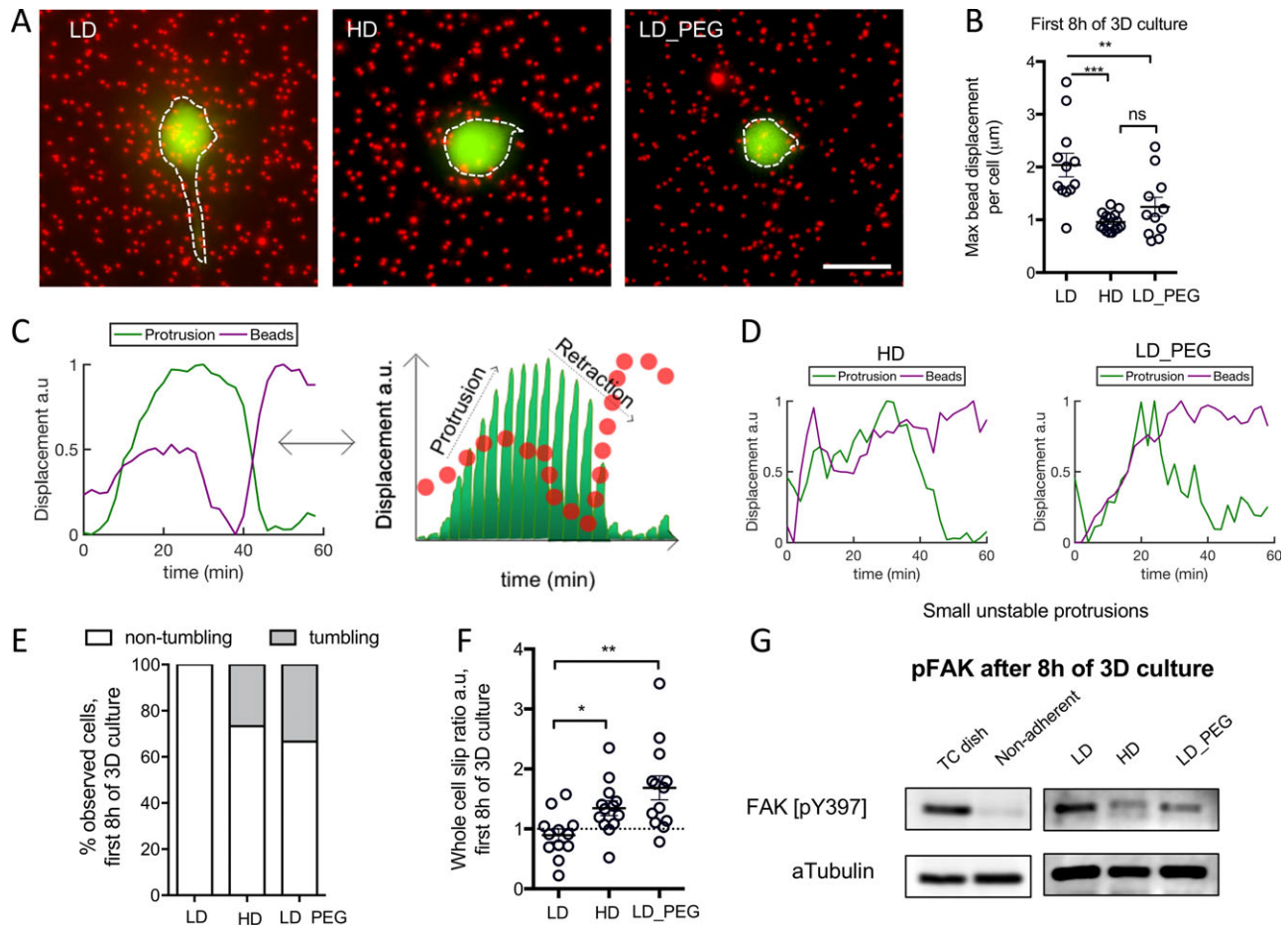

Figure 2. Short fiber architectures promote decreased cell-ECM adhesion. **A.** Representative maximum intensity projection fluorescent micrographs of GFP-expressing HT-1080 cells embedded in collagen matrices containing fluorescent microbeads. Scale bar 25 μm. **B.** Average max bead displacement around cells in the 3 different matrix architectures after 8 h of culture. **C.** A protrusion trajectory and mean trajectory of the top 25% moving beads highlights the pulling phenotype in LD matrix compared to **D.** confining HD and LD_PEG matrices. **E.** Quantification of cells showing a tumbling phenotype in the different matrix architectures. **F.** Whole cell slip ratio quantified from traction force microscopy data and single cell tracking after 8 h of culture (see methods). **G.** Western blot analysis of phosphorylated focal adhesion kinase (FAK) of cells cultured on 2D tissue culture treated dishes (lane 1), low attachment plates (lane 2), and the three collagen matrix architectures (lanes 3–5). Western blot images are representative of n = 3 experiments pooled after 8 h of culture. n = 3 biological replicates for each experiment, statistical significance described as *, **, *** for p≤0.05, p≤0.01, p≤0.001 respectively.

protrusions probed the surroundings (Figure 2D). Additionally, we observed that a fraction of the cells in the LD_PEG and HD collagen matrices exhibited a rotational tumbling or amoeboid phenotype, characterized by rapid cell movement without detectable bead movement around them (Figure 2E, Supplementary video 4), as opposed to the well-defined protrusion-associated deformations observed in LD matrices (Supplementary video 5). This suggested that cells adhesion was reduced.

To quantitatively characterize cell adhesion to the matrix, we simultaneously calculated the instantaneous velocity of the cells and instantaneous velocity of the beads adjacent to each cell. Cells well-coupled to the matrix produce bead movements roughly equivalent to the movement of the cell body. In contrast, beads around weakly adhered cells are expected to move at lower instantaneous rates than the cell body. Using this logic, we calculated the cell slip ratio as the ratio between the instantaneous velocity of cell body and the instantaneous velocity of the surrounding beads (Supplementary Figure 2E). We observed a significantly higher slip ratio (slip ratio >1) for cells embedded in LD_PEG and HD matrices compared to cells in LD (Figure 2F). In LD matrices, cells are well coupled to the matrix (slip ratio of ~1) or occasionally exhibited treadmilling on the matrix (slip ratio <1). Cells in all conditions displayed similar velocities (Supplementary Figure 2F). This suggested that reduced adhesion caused the decrease in bead displacement by cells in these matrices (Figure 2B).

To confirm that cells are unable to stabilize adhesions in the more confining LD_PEG and HD matrix architectures, we measured the amount of activated focal adhesion kinase (FAK) in the cells. Western blot analysis of FAK phosphorylated at tyrosine residue 397 (pFAK) confirmed a decrease in pFAK in cells embedded in the more confining matrices (Figure 2G). As a control, we compared this to pFAK levels in cells grown in non-adherent plates, which showed a significant decrease to almost undetectable levels, as has been previously reported [13, 14]. This suggested that more confining matrix architectures alter protrusion dynamics by reducing, but not eliminating, cell adhesion to the matrix.

Matrix induced low adhesion triggers metabolic and oxidative stress

It is well established that suspension culture in non-adherent conditions induces metabolic and oxidative stress [15, 16]. Since cells in confining matrices maintained a low level of adhesion and pFAK, we sought to determine the extent to which they experience metabolic and oxidative stress characteristic of a low-adhesion state. Phosphorylated FAK is an important negative regulator of Tuberous Sclerosis Complex 2 (TSC2) [17], which in turn negatively regulates the mammalian target of rapamycin (mTOR) pathway. It has been established that decreased pFAK can lead to increased TSC2 activity, which downregulates key mTOR target genes related to glycolysis, phosphate pentose pathway, and lipid biosynthesis pathways [18, 19]. Thus, we asked if the reduced levels of pFAK we observed in confining collagen matrices impacted this pathway. Analysis of RNA sequencing data revealed that mTOR target genes were largely downregulated in cells in more confining matrix conditions, consistent with their low levels of pFAK (Figure 3A). Further gene set enrichment analysis also revealed a decrease in the enrichment of TCA cycle and pyruvate metabolism pathways (Supplementary Figure 5) for cells growing in confining matrices compared to the non-confining LD condition.

Loss of attachment to ECM in suspension culture has also been shown to reduce glucose and glutamine uptake and promote accumulation of reactive oxygen species (ROS) due to reduced glucose flux through the pentose phosphate pathway (PPP) [15, 16, 20]. To further explore the parallels between how cells experience confining collagen compared to suspension culture, we asked whether glucose metabolism was altered. Measurement of glucose consumption and lactate production by cells at 24 h after collagen embedding revealed reduced glycolytic activity in confining matrices compared to non-confining matrices (Figure 3B-C). Cells consumed 10–20% less glucose and secreted 10–20% less lactate in confining matrices than in non-confining matrices. This biochemical state resembled that of cells cultured in non-adherent plates (Figure 3B-C). Glutamine uptake was also reduced in confining matrices (15–20% lower) as well as in cells in non-adherent plates (40% lower) (Figure 3D). Metabolic tracing of 1,2-^{13}C labeled glucose during the first 24 h of culture revealed that oxidative PPP (oxPPP) flux was reduced in confining conditions, consistent with decreased glucose uptake (Figure 3E). This suggested that cells in confinement experience redox stress similar to cells in suspension culture [15, 16, 20]. Relative shunting to the oxPPP was increased in confining conditions (Figure 3F), which has also been suggested to be a sign of redox stress [21]. Control experiments confirmed that nutrient diffusion was not different across the 3D culture conditions, and so cannot account for the stressed state (Supplementary Figure 6A-C). Cell division within the 24 h measurement window was also not statistically different across the conditions, and so does not account for differences in nutrient consumption (Supplementary Figure 6D). Taken together, these data indicate that confining collagen architectures are weakly-adhesive and induce metabolic changes in cells similar to that of anchorage-independent growth, which promotes downregulation of mTOR pathway target genes and a state of metabolic and oxidative stress. As a result, we hypothesized that cells in this condition may upregulate the expression of genes known to be ROS-responsive. In particular, heme oxygenase-1 (HO-1) is a gene that has been widely studied as a model oxidative stress-induced gene that serves as an endogenous antioxidant response system by catabolizing heme to produce bilirubin and carbon monoxide [22, 23]. Gene expression analysis of cells cultured in HD versus LD matrices 24 h after embedding revealed significantly increased expression of HO-1 (3.6-fold increase, p = 0.001, Figure 3G).

Cell adhesion is regulated by matrix degradation

Previous reports have shown that matrix crosslinking can be associated with a reduction in matrix degradability [24]. We wondered if confining architectures, i.e. smaller pores and shorter fibers, could also be associated with lowered degradability. Using an *in vitro* assay of collagen degradation with collagenase (Supplementary Figure 6E), we found that the more confining LD_PEG and HD matrices were significantly more resistant to degradation than the LD matrix (Figure 3H). As a control, we measured the diffusivity of molecular weight-matched fluorescent dextran and found no significant differences among the different collagen architectures (Supplementary Figure 6A-C).

Based on these results, we hypothesized that matrix degradability could modulate the ability of cells to create stable adhesions to the matrix. If this were the case, then inhibition of MMP activity would be expected to decrease cell adhesion. To test this, we embedded GFP-expressing HT-1080 cells in bead-laden matrices with the addition of a broad-spectrum MMP inhibitor
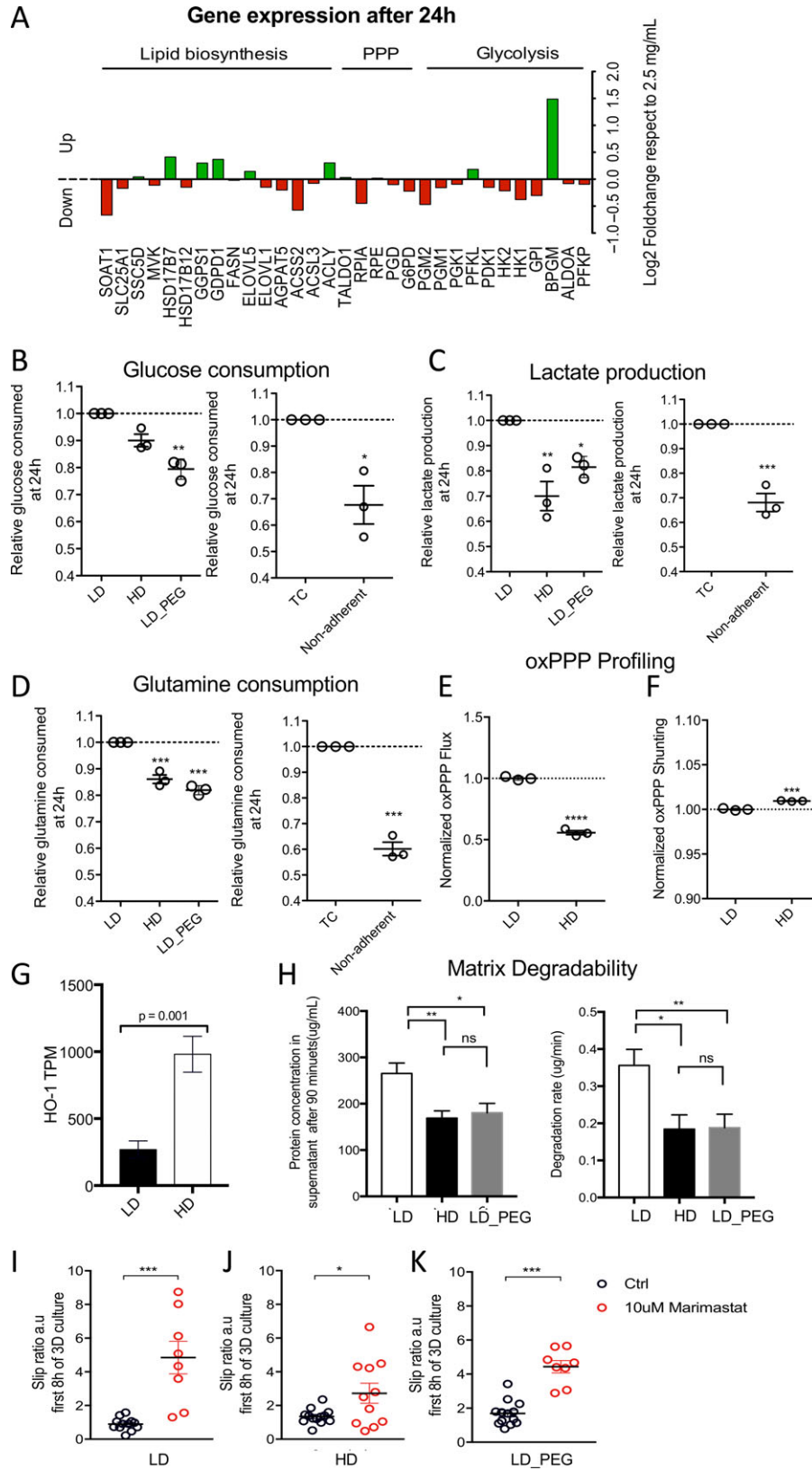
Figure 3. Confinement triggers metabolic and oxidative stress and is regulated by matrix degradation. **A.** Differential expression of genes targeted by the mTOR pathway in cells cultured in LD and HD matrices for 24 h. **B.** Relative glucose uptake. **C.** Relative lactate production and **D.** Relative glutamine uptake for cells growing in HD, LD_PEG, and LD matrices compared to tissue culture (TC) or non-adherent plates after 24 h. **E.** Profiling of oxidative Pentose Phosphate Pathway (oxPPP) measured by oxPPP flux and **F.** oxPPP shunting, normalized to LD condition, after 24 h. **G.** Differential expression of HO-1 by cells cultured in LD and HD after 24 h. **H.** Degradability of each collagen matrix condition, measured by protein content in supernatant after addition of collagenase. Total protein content in supernatant after 90 minutes of degradation (left) and degradation rate (right) **I.** Slip ratio of cells cultured in the presence of 10uM marimastat in LD, **J.** HD, and **K.** LD_PEG matrices after 8 h. n=>3 biological replicates for each experiment, statistical significance described as *, **, *** for p≤0.05, p≤0.01, p≤0.001 respectively.

(Marimastat) and measured the cell slip ratio as described above. MMP inhibition significantly increased cell slip across all matrix conditions (Figure 3I-K), indicating that matrix degradation activity is required for effective cell adhesion in 3D fibrilar collagen matrices.

Cells upregulate proteases, collagen catabolism, and Notch signaling in response to low attachment in confining architectures

Since MMP activity is required for successful cell-ECM coupling (Figure 3I-K), and cells in confining matrices eventually migrate to form collective networks (Figure 1E-G), we hypothesized that cells may upregulate proteolytic activity as a means of overcoming their low-adhesion state. Gene expression analysis of cells cultured in HD versus LD matrices at 24 h after embedding

showed significant increased expression of MMP-1, −2, and −14 (Figure 4A). To assess whether this transcriptional program was functional, we used dye quenched (DQ) collagen to measure pericellular matrix degradation patterns. DQ collagen emits strong green fluorescence when fibrils are cleaved and the attached fluorescein dye is no longer quenched [25]. Confocal imaging of the DQ collagen fluorescent signal 24 hours after 3D embedding revealed a significant increase in collagen degradation surrounding cells in confining architectures (Figure 4B-C). Very little collagen degradation was observed in LD matrices (Figure 4B-C), and no significant difference was observed between the DQ collagen intensity around the cell body versus protrusions in LD conditions (Supplementary Figure 7A).

Surprisingly, cells in confining matrices accumulated the fluorescent cleaved collagen in their cytoplasm (Figure 4B, white arrows), suggesting increased collagen internalization. Internalization
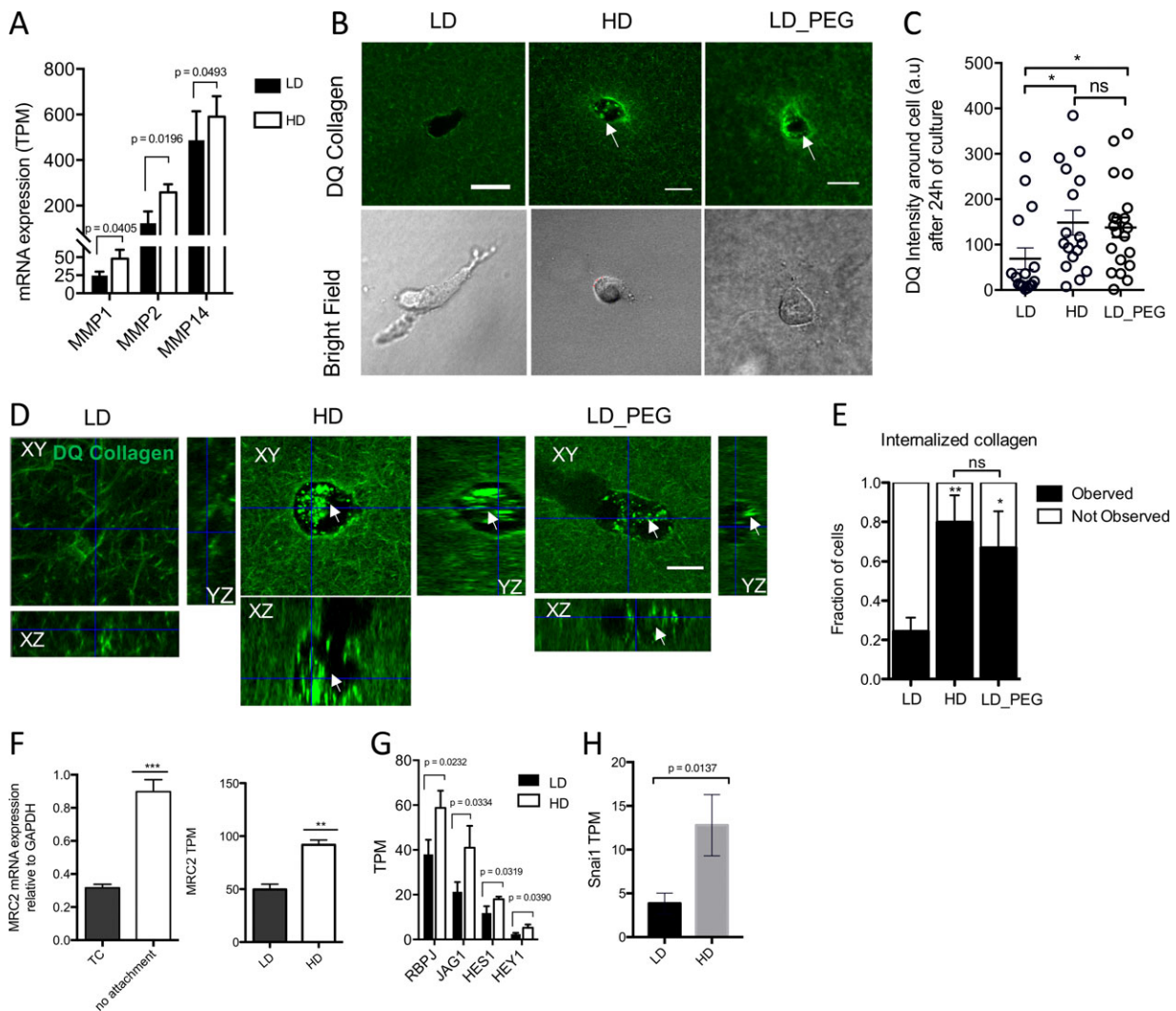

Figure 4. Crosslinked architecture promotes upregulation of proteases and Notch signaling. **A.** Differential MMP gene expression between cells cultured in LD and HD matrices. **B.** Fluorescent micrographs showing HT-1080 cells embedded in collagen matrices containing 100 ug/mL DQ-collagen type I (top row), white arrows point to areas around the cells with increased DQ collagen intensity, and respective bright field images (bottom row), scale bar 25 μm. **C.** Quantification of DQ intensity around cells cultured in the three different collagen architectures. **D.** Representative confocal z-stacks showing degraded collagen fragments internalized by cells (white arrows) in confining HD and LD_PEG matrices but not in the LD matrix, scale bar 15 μm **E.** Quantification of the fraction of cells where internalized collaged was observed **F.** MRC2 expression in cells cultured on tissue culture plates (TC) versus cells growing in low- attachment plates, LD, and HD collagen matrices. **G.** Differential expression of Notch pathway genes and **H.** Snai1 in cells cultured in LD and HD conditions. n=>3 biological replicates for each experiment, statistical significance described as *, **, *** for p≤0.05, p≤0.01, p≤0.001 respectively.

of fluorescent collagen was completely absent during the first few hours of cell-ECM interaction (Supplementary Figure 7B), suggesting internalization was an active process. High resolution z-stack imaging confirmed the intracellular localization of the internalized collagen (Figure 4D). This phenomenon was significantly more prevalent in cells cultured in the more confining LD_PEG and HD matrices (Figure 4E) compared to LD. Interestingly, gene expression analysis identified upregulation and significant enrichment of genes involved in collagen catabolic processes (23.8 fold enrichment, p = 3×10^{-6}) in cells embedded in confining matrices. Included in this set was MRC2, a gene encoding for Endo180, which is the main collagen endocytic receptor responsible for the internalization of degraded collagen [26, 27]. Using qRT-PCR, we also found this gene upregulated by cells growing in non-adherent plates (Figure 4F). However, these cells do not have access to extracellular collagen.

Genes in the Notch signaling pathway were also upregulated at 24 h and significantly enriched (26.52-fold enrichment, p = 0.03) by cells in confining matrices, including the Notch ligand JAG1, the transcription factor RBPJ, and Notch target genes HES1 and HEY1 (Figure 4G) [28]. Since cells are embedded sparsely, as single cells, this suggests ligand independent activation of Notch by the low-adhesion matrix conditions. Expression of Notch genes also suggest a potential molecular mechanism by which collective behaviors are initiated. The epithelial to mesenchymal transition (EMT) transcription factor SNAI1 (Snail1), was also upregulated by cells in confining matrices (3-fold increase, p=0.01, Figure 4H). SNAI1 is known to be a transcriptional target of the Notch intracellular domain.

Discussion

Previous studies by our group and others have characterized the transition from single to collective migration in response to confining 3D collagen environments [8, 9, 29, 30]. In the present study we set out to investigate the cell-ECM interactions that initiate this response. Our study reveals that changes in the fibrillar architecture of collagen, independent of stiffness or density, influence cell-ECM adhesive coupling. Fiber architectures that are more confining, i.e. smaller pores and shorter fibers, are less degradable, and this reduces cell adhesion resulting low-attachment stress. Low-attachment stress in 3D is characterized by reduced glycolytic activity and increased oxidative stress, which mimics stress induced by suspension culture or growth on non-adherent plates [15, 19]. Subsequent upregulation of genes involved in collagen catabolism, in combination with increased collagen degradation and internalization in 3D confining collagen, suggests that an endocytic pathway may play a role in overcoming oxidative and glycolytic stress associated with a 3D low-adhesion state. Interestingly, recent studies have shown that collagen internalization is upregulated in nutrient-starved cells, where collagen-derived proline is used as a substitute to fuel the TCA cycle and maintain cell survival [31]. Similarly, it has been shown that macro pinocytosis of proteins can be used as an amino acid supply by transformed cells [31, 32]. Symptoms of limited nutrient availability also include upregulation of MMPs [33, 34] and MRC2 [31], demonstrating that low adhesion and nutrient deprivation stress responses share several commonalities.

Collagen matrices with small pore sizes have previously been found to drive collective cell migration behavior and the upregulation of MMPs due to restriction of the nucleus [8, 29, 30]. However, matrix degradability and cell adhesion were not assessed in these earlier studies. Our study shows that a major difference in how cells interact with confining matrices is that they are unable to stabilize adhesions, which we show leads to metabolic and oxidative stress as well as ligand independent Notch activation. Other studies have linked destabilized adhesion to the upregulation of MMPs through oxidative stress induced NF-kB [35–38]. There is also evidence that Notch may be induced by ROS and NF-kB [39–41]. Further examination is necessary to determine whether these mechanistic links are involved in the induction of collective cancer cell migration. Ligand-dependent Notch signaling is known to regulate collective migration in normal tissue development by differentiating leader versus stalk cell phenotypes and also plays a role in tumor growth and metastasis [3,42–45]. The Notch intracellular domain transcriptionally regulates Snail1, which promotes metastasis, the cancer stem cell phenotype, and the regulation of chemo and immune resistance in cancer [46]. Our findings suggest a mechanism by which Notch signaling is initiated by ECM conditions.

Our study also demonstrates that matrix degradation activity is required for efficient adhesion in all of the 3D fibrillar collagen matrices we tested, not only the more confining conditions. Thus, cancer cells sense collagen degradability through adhesion signaling. Interestingly, the requirement for MMP activity in efficient cell-matrix adhesion offers a mechanistic explanation as to why MMP inhibitors and integrin blocking antibodies have the same effect of promoting mesenchymal to amoeboid switching in non-confining 3D collagen matrices [8, 47]. The dependence on matrix degradability for proper adhesion and traction has been reported previously in a synthetic hydrogel model system. In this case, mesenchymal stem cells (hMSCs) embedded in proteolysis-resistant hydrogels could not generate cytoskeleton tension and thus produced insignificant deformations to the surrounding matrix [48]. Recent studies show that MMP proteolytic activity is also required for cell adhesion and spreading on 2D substrates [49]. Our study demonstrates the role of degradability in the context of fibrillar 3D collagen.

The requirement for matrix degradation in cell-ECM adhesion in fibrillar collagen I suggests that either binding sites must be revealed through degradation or that cells need to bundle and reorganize fibers to create stable adhesions. High- and low-affinity integrin-binding motifs are present in collagen fibrils [50] and could be differentially accessible based on architecture. Changes in the complex molecular assembly of bundled triple helices within the collagen fibril can make essential ligand binding sites cryptic or hidden from the molecular surface [50]. Indeed, it has been shown that collagen binding motifs can be differentially presented depending of fibril conformation [51]. It is believed that cell-collagen interactions are regulated by cryptic binding motifs being exposed upon structural reorganization or degradation of the fibril. Our results suggest that structural reorganization and degradation are linked. *In vivo*, deposition of collagen that is resistant to degradation occurs in fetal tissues [52, 53], fibrosis [54–56], and cancer [57–61]. Thus, the collagen-induced low adhesion state we identified herein may be relevant to the onset and progression of these processes. In the context of cancer, it may even prime or select for cells capable of surviving low-adhesion conditions during hematogenous circulation and metastasis.

Supplementary data

Supplementary data is available at *INTBIO* online.

References

1. Cheung KJ, Ewald AJ. A collective route to metastasis: seeding by tumor cell clusters. *Science* 2016;**352**:167–169.
2. Massagué J, Obenauf AC. Metastatic colonization by circulating tumour cells. *Nature* 2016;**529**:298.
3. Cheung KJ. Polyclonal breast cancer metastases arise from collective dissemination of keratin 14-expressing tumor cell clusters. *Proc Natl Acad Sci U S A* 2016;**113**:E854–E863.
4. Shi W. Facile tumor spheroids formation in large quantity with controllable size and high uniformity. *Sci Rep* 2018;**8**:6837.
5. Loessner D. Bioengineered 3D platform to explore cell–ECM interactions and drug resistance of epithelial ovarian cancer cells. *Biomaterials* 2010;**31**:8494–8506.
6. Aceto N. Circulating tumor cell clusters are oligoclonal precursors of breast cancer metastasis. *Cell* 2014;**158**:1110–1122.
7. Paul CD, Mistriotis P, Konstantopoulos K. Cancer cell motility: lessons from migration in confined spaces. *Nat Rev Cancer* 2016;**17**:131.
8. Wolf K. Physical limits of cell migration: Control by ECM space and nuclear deformation and tuning by proteolysis and traction force. *J Cell Biol* 2013;**201**:1069–1084. doi:10.1083/jcb.201210152.
9. Velez D. 3D collagen architecture induces a conserved migratory and transcriptional response linked to vasculogenic mimicry. *Nat Commun* 2017;**8**:1651.
10. Trappmann B. Matrix degradability controls multicellularity of 3D cell migration. *Nature communications* 2017;**8**:371.
11. Ranamukhaarachchi SK. Macromolecular crowding tunes 3D collagen architecture and cell morphogenesis. *Biomater Sci* 2019;**7**:618–633. doi:10.1039/c8bm01188e.
12. Wen JH. Interplay of matrix stiffness and protein tethering in stem cell differentiation. *Nat Mater* 2014;**13**:979.
13. Kornberg L, Earp HS, Parsons JT et al. Cell adhesion or integrin clustering increases phosphorylation of a focal adhesion-associated tyrosine kinase. *J Biol Chem* 1992;**267**:23439–23442.
14. Hamadi A. Regulation of focal adhesion dynamics and disassembly by phosphorylation of FAK at tyrosine 397. *J Cell Sci* 2005;**118**:4415–4425.
15. Schafer ZT. Antioxidant and oncogene rescue of metabolic defects caused by loss of matrix attachment. *Nature* 2009;**461**:109.
16. Jiang L. Reductive carboxylation supports redox homeostasis during anchorage-independent growth. *Nature* 2016;**532**: 255.
17. Gan B, Yoo Y, Guan J-L. Association of focal adhesion kinase with tuberous sclerosis complex 2 in the regulation of s6 kinase activation and cell growth. *J Biol Chem* 2006;**281**: 37321–37329.
18. Düvel K. Activation of a metabolic gene regulatory network downstream of mTOR complex 1. *Molecular cell* 2010;**39**:171–183.
19. Grassian A, Coloff J, Brugge J. Extracellular matrix regulation of metabolism and implications for tumorigenesis. *Cold Spring Harb Symp Quant Biol* 2011;**76**:313–324. doi:10.1101/sqb.2011.76.010967.
20. Grassian AR, Metallo CM, Coloff JL et al. Erk regulation of pyruvate dehydrogenase flux through PDK4 modulates cell proliferation. . *Genes & Development* 2011;**25**:1716–1733.
21. Anastasiou D. Inhibition of pyruvate kinase M2 by reactive oxygen species contributes to cellular antioxidant responses. *Science* 2011;**334**:1278–1283. doi:10.1126/science.1211485. Epub 2011 Nov 3.
22. Turkseven S. Antioxidant mechanism of heme oxygenase-1 involves an increase in superoxide dismutase and catalase in experimental diabetes. *Am J Physiol Heart Circ Physiol* 2005;**289**:H701–707. doi:10.1152/ajpheart.00024.2005.
23. Parfenova H, Leffler CW, Basuroy S et al. Antioxidant roles of heme oxygenase, carbon monoxide, and bilirubin in cerebral circulation during seizures. *J Cereb Blood Flow Metab* 2012;**32**: 1024–1034. doi:10.1038/jcbfm.2012.13. Epub 2012 Feb 22.
24. Flynn BP. Mechanical strain stabilizes reconstituted collagen fibrils against enzymatic degradation by mammalian collagenase matrix metalloproteinase 8 (MMP-8). *PLoS One* 2010; **5**:e12337.
25. Jedeszko C, Sameni M, Olive MB et al. Visualizing protease activity in living cells: from two dimensions to four dimensions. *Curr Protoc Cell Biol* 2008;**39**:4.20. 21–24.20. 15.
26. Melander MC, Jürgensen HJ, Madsen DH et al. The collagen receptor uPARAP/Endo180 in tissue degradation and cancer. *Int J Oncol* 2015;**47**:1177–1188.
27. Madsen DH. Extracellular collagenases and the endocytic receptor, urokinase plasminogen activator receptor-associated protein/Endo180, cooperate in fibroblast-mediated collagen degradation. *J Biol Chem* 2007;**282**:27037–27045.
28. D'Souza B, Meloty-Kapella L, Weinmaster G. Canonical and non-canonical notch ligands. *Curr Top Dev Biol* 2010;**92**: 73–129. doi:10.1016/s0070-2153(10)92003-6.
29. Haeger A, Krause M, Wolf K et al. Cell jamming: collective invasion of mesenchymal tumor cells imposed by tissue confinement. *Bioch et Biophys Acta* 2014;**1840**:2386–2395. doi:10.1016/j.bbagen.2014.03.020.
30. Wolf K, Friedl P. Extracellular matrix determinants of proteolytic and non-proteolytic cell migration. *Trends Cell Biol* 2011;**21**:736–744.
31. Olivares O. Collagen-derived proline promotes pancreatic ductal adenocarcinoma cell survival under nutrient limited conditions. *Nat Commun* 2017;**8**:16031.

32. Commisso C. Macropinocytosis of protein is an amino acid supply route in Ras-transformed cells. *Nature* 2013;**497**:633.

33. Liu T. CD133+ cells with cancer stem cell characteristics associates with vasculogenic mimicry in triple-negative breast cancer. *Oncogene* 2013;**32**:544–553.

34. Gingras D, Page M, Annabi B et al. Rapid activation of matrix metalloproteinase-2 by glioma cells occurs through a post-translational MT1-MMP-dependent mechanism. *Bioch et Biophys Acta* 2000;**1497**:341–350.

35. Morgan MJ, Liu Z.-G. Crosstalk of reactive oxygen species and NF-κB signaling. *Cell Res* 2011;**21**:103.

36. Lu Y, Wahl LM. Oxidative stress augments the production of matrix metalloproteinase-1, cyclooxygenase-2, and prostaglandin E2 through enhancement of NF-κB activity in lipopolysaccharide-activated human primary monocytes. *J Immunol* 2005;**175**:5423–5429.

37. Yan C, Boyd DD. Regulation of matrix metalloproteinase gene expression. *J Cell Physiol* 2007;**211**:19–26.

38. Kratsovnik E, Bromberg Y, Sperling O et al. Oxidative stress activates transcription factor NF-κB-mediated protective signaling in primary rat neuronal cultures. *J Mol Neurosci* 2005;**26**:27–32.

39. Maniati E. Crosstalk between the canonical NF-κB and Notch signaling pathways inhibits Pparγ expression and promotes pancreatic cancer progression in mice. *J Clin Investig* 2011;**121**:4685–4699.

40. Coant N. NADPH oxidase 1 modulates WNT and NOTCH1 signaling to control the fate of proliferative progenitor cells in the colon. *Mol Cell Biol* 2010;**30**:2636–2650.

41. Caliceti C, Nigro P, Rizzo P et al. ROS, Notch, and Wnt signaling pathways: crosstalk between three major regulators of cardiovascular biology. *BioMed Res Int* 2014;**2014**.

42. Theveneau E, Linker C. Leaders in collective migration: are front cells really endowed with a particular set of skills? *F1000Research* 2017;**6**.

43. Riahi R. Notch1–Dll4 signalling and mechanical force regulate leader cell formation during collective cell migration. *Nat Commun* 2015;**6**:6556.

44. Sonoshita M Promotion of colorectal cancer invasion and metastasis through activation of NOTCH–DAB1–ABL–RHOGEF protein TRIO. *Cancer discovery* (2014).

45. Fischer A, Schumacher N, Maier M et al. The Notch target genes Hey1 and Hey2 are required for embryonic vascular development. *Genes & Development* 2004;**18**:901–911.

46. Kaufhold S, Bonavida B. Central role of Snail1 in the regulation of EMT and resistance in cancer: a target for therapeutic intervention. *Journal of Experimental & Clinical Cancer Research: CR* 2014;**33**:62. doi:10.1186/s13046–014–0062–0.

47. Wolf K. Multi-step pericellular proteolysis controls the transition from individual to collective cancer cell invasion. *Nature Cell Biology* 2007;**9**:893.

48. Khetan S. Degradation-mediated cellular traction directs stem cell fate in covalently crosslinked three-dimensional hydrogels. *Nature Materials* 2013;**12**:458.

49. Das A, Monteiro M, Barai A et al. MMP proteolytic activity regulates cancer invasiveness by modulating integrins. *Sci Rep* 2017;**7**:14219. doi:10.1038/s41598–017–14340-w.

50. Hoop CL, Zhu J, Nunes AM et al. Revealing accessibility of cryptic protein binding sites within the functional collagen fibril. *Biomolecules* 2017;**7**. doi:10.3390/biom7040076.

51. Rosini S. Thrombospondin-1 promotes matrix homeostasis by interacting with collagen and lysyl oxidase precursors and collagen cross-linking sites. *Sci. Signal.* 11 2018:eaar2566.

52. Jimenez SA, Bashey RI, Benditt M et al. Identification of collagen alpha1(I) trimer in embryonic chick tendons and calvaria. *Biochemical and Biophysical Research Communications* 1977;**78**:1354–1361.

53. Lesot H, Karcher-Djuricic V, Ruch JV. Synthesis of collagen type I, type I trimer and type III by embryonic mouse dental epithelial and mesenchymal cells in vitro. *Biochimica et Biophysica Acta* 1981;**656**:206–212.

54. Narayanan AS, Page RC, Meyers DF. Characterization of collagens of diseased human gingiva. *Biochemistry* 1980;**19**:5037–5043.

55. Rojkind M, Giambrone MA, Biempica L. Collagen types in normal and cirrhotic liver. *Gastroenterology* 1979;**76**:710–719.

56. Ehrlich HP, Brown H, White BS. Evidence for type V and I trimer collagens in Dupuytren's Contracture palmar fascia. *Biochemical Medicine* 1982;**28**:273–284.

57. Makareeva E. Carcinomas contain a matrix metalloproteinase-resistant isoform of type I collagen exerting selective support to invasion. *Cancer Research* 2010;**70**:4366–4374. doi:10.1158/0008–5472.can-09–4057.

58. DeClerck YA, Bomann ET, Spengler BA et al. Differential collagen biosynthesis by human neuroblastoma cell variants. *Cancer Research* 1987;**47**:6505–6510.

59. Rupard JH, Dimari SJ, Damjanov I et al. Synthesis of type I homotrimer collagen molecules by cultured human lung adenocarcinoma cells. *The American Journal of Pathology* 1988;**133**:316–326.

60. Little CD, Church RL, Miller RA et al. Procollagen and collagen produced by a teratocarcinoma-derived cell line, TSD4: evidence for a new molecular form of collagen. *Cell* 1977;**10**:287–295.

61. Minafra S, Luparello C, Rallo F et al. Collagen biosynthesis by a breast carcinoma cell strain and biopsy fragments of the primary tumour. *Cell Biology International Reports* 1988;**12**:895–905.

62. Fraley SI. A distinctive role for focal adhesion proteins in three-dimensional cell motility. *Nature Cell Biology* 2010;**12**:598–604.

63. Fraley SI, Feng Y, Giri A et al. Dimensional and temporal controls of three-dimensional cell migration by zyxin and binding partners. *Nature Communications* 2012;**3**:719. doi:10.1038/ncomms1711.

64. Fraley SI. Three-dimensional matrix fiber alignment modulates cell migration and MT1-MMP utility by spatially and temporally directing protrusions. *Sci Rep* 2015;**5**:14580. doi:10.1038/srep14580.

65. Radmacher M, Fritz M, Hansma PK. Imaging soft samples with the atomic force microscope: gelatin in water and propanol. *Biophys J* 1995;**69**:264–270. doi:10.1016/s0006–3495(95)79897–6.

66. Engler AJ, Rehfeldt F, Sen S et al. Microtissue elasticity: measurements by atomic force microscopy and its influence on cell differentiation. *Methods in Cell Biology* 2007;**83**:521–545. doi:10.1016/s0091–679x(07)83022–6.

67. Engler AJ, Richert L, Wong JY et al. Surface probe measurements of the elasticity of sectioned tissue, thin gels and polyelectrolyte multilayer films: Correlations between substrate stiffness and cell adhesion. *Surface Science* 2004;**570**:142–154. doi:doi:10.1016/j.susc.2004.06.179.

68. Viswanathan P, Chirasatitsin S, Ngamkham K et al. Cell instructive microporous scaffolds through interface engineering. *Journal of the American Chemical Society* 2012;**134**:20103–20109.

69. Bredfeldt JS. Automated quantification of aligned collagen for human breast carcinoma prognosis. *Journal of Pathology Informatics* 2014;**5**.

70. Bredfeldt JS. Computational segmentation of collagen fibers from second-harmonic generation images of breast cancer. *Journal of Biomedical Optics* 2014;**19**:016007.

71. Langmead B, Salzberg SL. Fast gapped-read alignment with Bowtie 2. *Nature Methods* 2012;**9**:357–359. doi:10.1038/nmeth.1923.

72. Roberts A, Pachter L. Streaming fragment assignment for real-time analysis of sequencing experiments. *Nature Methods* 2013;**10**:71–73. doi:10.1038/nmeth.2251.

73. Fernandez CA, Des Rosiers C, Previs SF et al. Correction of 13C mass isotopomer distributions for natural stable isotope abundance. *Journal of Mass Spectrometry: JMS* 1996;**31**: 255–262. doi:10.1002/(sici)1096–9888(199603)31:3<255::aid-jms290>3.0.co;2–3.

74. Capella-Monsonís H, Coentro JQ, Graceffa V et al. An experimental toolbox for characterization of mammalian collagen type I in biological specimens. *Nature Protocols* 2018;**13**:507.